Ultrasound in Med. & Biol., Vol. 47, No. 9, pp. 2734–2748, 2021

0301-5629/$ - see front matter

https://doi.org/10.1016/j.ultrasmedbio.2021.05.010

● *Original Contribution*

EFFECT OF SKULL POROUS TRABECULAR STRUCTURE ON TRANSCRANIAL ULTRASOUND IMAGING IN THE PRESENCE OF ELASTIC WAVE MODE CONVERSION AT VARYING INCIDENCE ANGLE

BOWEN JING,* and BROOKS D. LINDSEY*,†

* Wallace H. Coulter Department of Biomedical Engineering, Georgia Institute of Technology and Emory University, Atlanta, Georgia, USA; and † School of Electrical and Computer Engineering, Georgia Institute of Technology, Atlanta, Georgia, USA

(*Received* 15 *December* 2020; *revised* 4 *May* 2021; *in final form* 7 *May* 2021)

Abstract—With the advancement of aberration correction techniques, transcranial ultrasound imaging has exhibited great potential in applications such as imaging neurological function and guiding therapeutic ultrasound. However, the feasibility of transcranial imaging varies among individuals because of the differences in skull acoustic properties. To better understand the fundamental mechanisms underlying the variation in imaging performance, the effect of the structure of the porous trabecular bone on transcranial imaging performance (*i.e.,* target localization errors and resolution) was investigated for the first time through the use of elastic wave simulations and experiments. Simulation studies using high-resolution computed tomography data from *ex vivo* skull samples revealed that imaging at large incidence angles reduced the target localization error for skulls having low porosity; however, as skull porosity increased, large angles of incidence resulted in degradation of resolution and increased target localization errors. Experimental results indicate that imaging at normal incidence introduced a localization error of 1.85 ± 0.10 mm, while imaging at a large incidence angle (40°) resulted in an increased localization error of 6.54 ± 1.33 mm and caused a single point target to no longer appear as a single, coherent target in the resulting image, which is consistent with simulation results. This first investigation of the effects of skull microstructure on transcranial ultrasound imaging indicates that imaging performance is highly dependent on the porosity of the skull, particularly at non-normal angles of incidence. (E-mail: brooks.lindsey@bme.gatech.edu) **© 2021 World Federation for Ultrasound in Medicine & Biology. All rights reserved.**

Key Words: **Incidence angle, Longitudinal wave, Mode conversion, Porosity, Shear wave, Trabecular bone, Transcranial ultrasound.**

INTRODUCTION

Transcranial ultrasound imaging has been reported to be a useful tool not only for assessment of neurological function and cerebrovascular diseases but also for real-time monitoring and guidance of transcranial focused ultrasound therapy (Qiu et al. 2020). Because of its portability and real-time imaging capability, ultrasound has been used for imaging during early stages after acute stroke events (Holscher et al. 2008; Schlachetzki et al. 2012; Herzberg et al. 2014; Antipova et al. 2020). Blood flow to major arteries such as those of the circle of Willis and internal carotid arteries can be imaged and quantified using 2-D or 3-D ultrasound Doppler imaging through the temporal bone window (Tsuchiya et al. 1991; Lyden and Nelson 1997; Krejza et al. 1999; Lindsey et al. 2011, 2013; Lindsey and Smith 2013). Microbubble contrast agents have also been used to enhance the ability to quantify blood flow and map spatial and temporal perfusion of the brain (Wiesmann et al. 2004; Bartels et al. 2005; Della Martina et al. 2005). The emergence of high-frame-rate ultrasound imaging techniques has enabled imaging and quantification of the hemodynamic response of regional brain tissue caused by variation in neurological activity with subsecond temporal resolution (Errico et al. 2016; Imbault et al. 2017). Furthermore, the development of super-resolution imaging techniques has enabled the visualization of the vasculature through the skull with spatial resolution beyond the diffraction limit (O'Reilly and Hynynen 2013; Soulioti et al. 2020).

In addition to its use as a diagnostic tool, transcranial ultrasound imaging has been found to be a useful tool for

Address correspondence to: Brooks D. Lindsey, Wallace H. Coulter Department of Biomedical Engineering, Georgia Institute of Technology and Emory University, 2107 Whitaker Building, 313 Ferst Drive, Atlanta, GA 30332, USA. E-mail: brooks.lindsey@bme.gatech.edu

monitoring and guiding transcranial ultrasound therapy by both visualizing and quantifying ultrasound-induced cavitation. Utilizing acoustic cavitation emissions in the form of shock waves, Sukovich et al. (2020) reported the capability of transcranial ultrasound imaging of cavitation events during transcranial histotripsy. Moreover, by using passive cavitation imaging techniques, researchers have been able to transcranially image cavitation events (Arvanitis and McDannold 2013; O'Reilly et al. 2014), map the ultrasound-induced blood−brain barrier opening (Sun et al. 2017; Burgess et al. 2018; Jones et al. 2018; Wu et al. 2018; Yang et al. 2019; Lin et al. 2020) and monitor non-thermal brain tissue ablation (Xu et al. 2019; Jones et al. 2020). Recent advances in 2-D array design have enabled 3-D transcranial focusing (Chaplin et al. 2018; Wu et al. 2021) and mapping of the acoustic emissions originating from ultrasound-induced cavitation (Deng et al. 2016; Crake et al. 2018; Liu et al. 2018; Sukovich et al. 2020). In addition to monitoring cavitation, transcranial acoustoelectric imaging has been used for monitoring directional current in deep brain stimulation (Preston et al. 2020).

Transcranial imaging relies on transmission of sufficient acoustic amplitude through the skull in both directions for pulse-echo imaging. Because of spatially varying speed of sound in the tissues (especially in the skull), aberration is introduced that degrades the imaging performance (Ivancevich et al. 2008; Jones et al. 2013; Lindsey and Smith 2013). Thus, transcranial imaging often requires additional steps to correct for aberration by accounting for the velocity of the longitudinal wave in the skull, which is significantly higher than that in soft tissues (Clement and Hynynen 2002; Aubry et al. 2003; Ivancevich et al. 2008; Lindsey et al. 2011, 2013; Jing et al. 2012; Jones et al. 2013; Lindsey and Smith 2013; Kyriakou et al. 2015; Jiang et al. 2019; Schoen and Arvanitis 2020). In these studies, the shear waves, which are much slower than the longitudinal waves, are usually neglected. This assumes that longitudinal-to-shear mode conversion, which occurs at all interfaces between the skull and soft tissues (*i.e.,* skin, brain, bone marrow), is negligible when the incidence angle is close to normal. However, the assumption of negligible mode conversion is not always valid when the angle is increased for targets near the skull (Pichardo and Hynynen 2007); for cases of irregular bone−soft tissue interfaces, that is, marrow-filled pores, in the trabecular bone layer (Robertson et al. 2018); or for phased array imaging at larger angles of incidence (Vignon et al. 2010; Lucht et al. 2013; Lindsey and Smith 2014). Furthermore, because of the unique boundary conditions, the human skull also supports various modes of Lamb waves at different phase velocities (Estrada et al. 2018). Recently, researchers have determined the potential for using Lamb waves for characterizing the skull (Mazzotti et al. 2021a) or as a means of coupling acoustic energy into the brain (Firouzi et al. 2017; Mazzotti et al. 2021b).

Alternatively, longitudinal-to-shear mode conversion has been reported to have benefits for transcranial acoustic focusing and aberration reduction in multiple *ex vivo* human skulls by transmitting ultrasound waves at large angles of incidence (Clement et al. 2004; White et al. 2006). This reduced aberration is believed to be owing primarily to the significant reduction in the mismatch in the wave velocity between the skull and brain tissue when the shear wave mode dominates in the skull at an incidence angle above Snell's critical angle (*i.e.,* 25°−30°; Clement et al. 2004; White et al. 2006; Yousefi et al. 2009; Vignon et al. 2010; Lucht et al. 2013; Lindsey and Smith 2014). However, shear wave mode conversion imaging does not always improve transcranial image quality for some individual skulls, even though several methods such as coded excitation (Yousefi et al. 2009), subharmonic imaging (Lucht et al. 2013) and ultrafast Doppler imaging (Jing et al. 2020) have been used to compensate for acoustic attenuation, improving imaging signal-to-noise ratio (SNR) and the ability to detect coherent targets through the skull. Some individual skulls appear to be more difficult to image through for reasons that are not fully explained by SNR alone (Marinoni et al. 1997; Yousefi et al. 2009; Lindsey et al. 2013; Lucht et al. 2013; Gahn et al. 2000). In fact, the assumption of the dominance of shear wave propagation at large incidence angles is not always accurate because of the presence of the bone−soft tissue interfaces (porous structure) inside the skull, which has not been fully investigated because of the high resolution required to resolve the fine, heterogenous microstructure within the center layer (trabecular bone) of the skull (Pichardo et al. 2017). Although there have been studies of elastic ultrasound propagation through skulls using numerical simulation with finely resolved trabecular heterogeneity (Liu 2012; Pinton et al. 2012; Robertson et al. 2018), the effect of the porous structure of the human skull on transcranial focusing or pulse-echo imaging at various incidence angles in the presence of longitudinal-to-shear mode conversion has not been investigated.

In this study, transcranial pulse-echo imaging performance is examined via simulations and experimental studies with *ex vivo* human skull samples, with the goal of developing an initial understanding of the effects of skull microstructure on image quality in the presence of elastic wave mode conversion at various incidence angles. To our knowledge, this is the first investigation of the effects of skull microstructure on transcranial ultrasound imaging, at either normal or varying angles of incidence. Numerical acoustic simulations of

transcranial imaging were conducted using high-resolution micro-computed tomography (microCT) data of the *ex vivo* human skull. Transcranial imaging was simulated at different frequency ranges and through different parts of the skull to mimic both transcranial monitoring of ultrasound therapy and transcranial Doppler imaging. For the simulation of transcranial monitoring of therapeutic ultrasound, low-frequency (1 MHz) transmission was performed through skull plates 6 and 10 mm thick. Transcranial Doppler imaging was simulated with transmission in the range 1.5−3 MHz for imaging through an ~3-mm-thick temporal bone window. Experimental studies in the range 1.5−3 MHz were conducted to validate findings in the simulation study. In these studies, a differential imaging method with a long ensemble was used to minimize the influence of electronic noise to investigate only phenomena of acoustic origins in transcranial pulse-echo imaging.

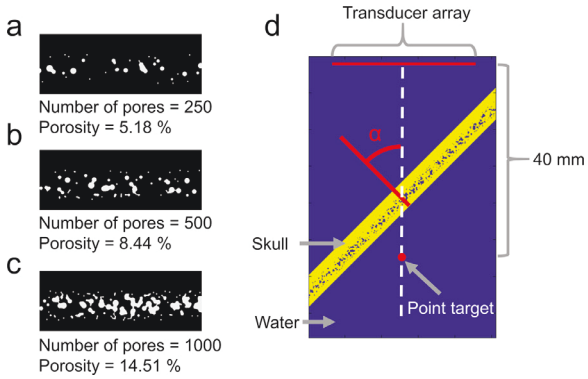

Fig. 1. (a−c) Simulation setup for transcranial imaging through skull plates at three different levels of porosity: (a) 5.18%, (b) 8.44%, (c) 14.51%. (d) The skull plate was placed in the water with a varying angle (α) to simulate transcranial imaging at various angles of incidence (*i.e.,* 0˚, 15˚, 30˚, 40˚). A point target was placed 10 mm below the skull. The distance from the transducer array to the point target is 40 mm.

METHODS

Simulation study

Transcranial imaging numerical simulation methods. In this study, the K-wave simulation toolbox (Treeby et al. 2014) based on the *k*-space pseudo-spectral method was used to simulate the propagation of ultrasound waves through the skull. Because of its scale, the simulation was performed in 2-D space. The thickness of the perfect matching layer, which was used to minimize periodic waves and reflection in the *k*-space computation domain, was set to be 20 grid points.

A 100-element transducer array (0.3-mm pitch) was simulated for both transmitting and receiving. The performance of transcranial imaging was evaluated at varying angles of incidence (*i.e.,* 0˚, 15˚, 30˚ and 40˚), resulting in the ultrasound waves traveling in different wave modes through the skull.

A sub-wavelength point scatterer was used as a simple target to provide straightforward feedback on the performance of pulse-echo ultrasound imaging through skull with varying angle, frequency and skull properties. To clearly measure the effect of these variables on imaging of the brain, a strong reflective point target with an acoustic impedance of 47.7×10^6 Rayl and a diameter of 0.25 mm was placed 40 mm away from the transducer. The skull plate was placed between the transducer and the target at a distance of 30 mm from the transducer surface (Figs. 1d and 2e). The reason the transducer was not attached directly to the skull was to ensure enough space for the skull to rotate with respect to the transducer surface. By characterizing the imaging response to a simple, highly scattering target positioned in the brain, the effect of the independent variables can be analyzed, allowing for extrapolation of these results to cases with diffuse, speckle-producing targets typically found in the brain.

For simulated transcranial images, two frames of images were acquired: with and without the point target. Each image was obtained by transmitting a plane wave. The final image was obtained by subtracting the beamformed radiofrequency data simulated without the point target from the data with the target to discard the skull signal, which is similar to clutter filtering in Doppler imaging. A delay-and-sum approach was used for reconstructing images. For the delay calculation for delay-and-sum beamforming, the speed of sound was assumed to be a constant, equal to the speed of sound in water. Imaging performance was evaluated without using any aberration correction method to examine the effect of varying incidence angle (*i.e.,* up to large angles to induce mode conversion) on the accuracy of single-target localization.

Simulation using different porous skull samples. To simulate different scenarios in transcranial ultrasound imaging, three different skull samples were included in the simulation. The skull acoustic properties are listed in Table 1 and are in accordance with previous studies of acoustic absorption in the skull (Pinton et al. 2012). The tissue in the pores and brain is simplified as water, which is consistent with the experimental studies using an *ex vivo* skull.

First, to investigate the effect of porosity on transcranial imaging, ideal bone plate phantoms with a flat surface were generated artificially. The thicknesses of the outer cortical table, inner cortical table and center trabecular layer were set to be 2, 1 and 3 mm, respectively. Three levels of porosity were simulated using the method described in a recent study (Mazzotti et al. 2021b),

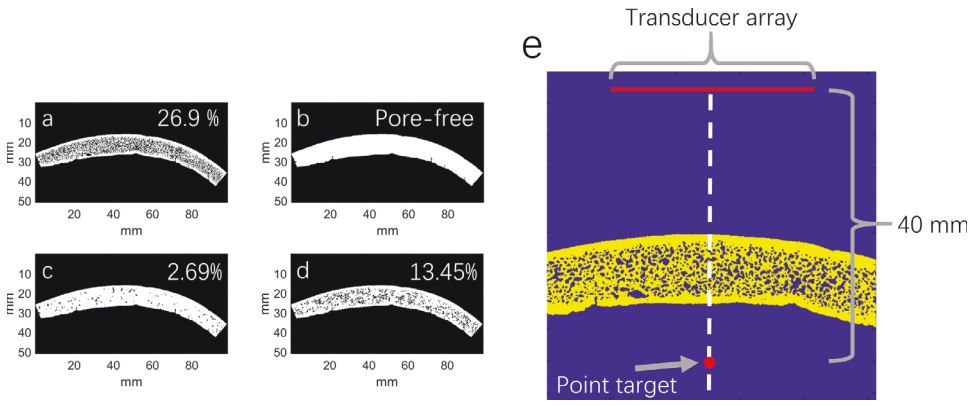

Fig. 2. Simulation of transcranial imaging using micro-computed tomography data of an *ex vivo* human skull piece. (a–d) Four levels of porosity were simulated: (a) original skull with all naturally occurring pores (porosity of 26.9 %); (b) the skull with all the pores removed; (c) the skull with a porosity of 2.69%; (b) the skull with a porosity of 13.45%. (e) The skull was placed in the water to simulate transcranial imaging at various incidence angles (*i.e.,* 0˚, 15˚, 30˚, 40˚). A point target was placed 10 mm below the skull. The distance from the transducer array to the point target is 40 mm.

Table 1. Acoustic properties of the skull used in the simulation

	Cortical bone	Water (filled pores)
Density (kg/m^3)	1850	1000
Longitudinal wave speed (m/s)	3000	1540
Shear wave speed (m/s)	1500	
Longitudinal absorption (dB/cm/MHz^2)	2.7	0.002
Shear absorption (dB/cm/MHz^2)	5.4	

including 5.18% (250 pores), 8.44% (500 pores) and 14.51% (1000 pores), as illustrated in Figure 1. The porosity was calculated based on the ratio between the porous area and the total area of the bone. In this part of the study, ultrasound images were simulated at a low frequency of 1 MHz with minimal absorption. The 2-D grid spacing was 0.05 mm, which ensures that the minimum number of spatial grid points per wavelength was larger than 25 to minimize the staircase error (Robertson et al. 2017a, 2017b). The Courant–Friedrichs–Lewy number was set to be 0.1 to ensure a stable numerical solution.

Next, to simulate low-frequency ultrasound imaging through actual human skulls (*i.e.,* for cavitation mapping) (Arvanitis and McDannold 2013; Jones et al. 2013; Crake et al. 2018; Sukovich et al. 2020), a second skull sample for simulations was generated from an ~10-mm-thick parietal bone scanned using high-resolution microCT at a voxel size of 0.048 mm. A 2-D cross-section of the skull was obtained. The CT image was segmented to preserve the pores of the trabecular bone, as illustrated in Figure 2. To investigate the effect of porosity, the porosity was varied by randomly discarding pores. The original porosity of the skull sample was 26.9% (Fig. 2a) based on the area of pores in the 2-D cross-section. By randomly discarding half of the pores, five skull samples with a porosity of 13.45% (Fig. 2d) were generated. By discarding 90% of pores, five skull samples with a porosity of 2.69% (Fig 2c) were generated. By discarding all the pores in the skull, a single sample of a pore-free skull was generated (Fig. 2b). The binarized image of the skull was used to simulate ultrasound propagation. The acoustic properties of the bone were kept the same as those in the first simulation. In this part of the study, ultrasound images were simulated at 1 MHz.

In the third part of the simulation study, transcranial imaging through the temporal acoustic window (~3 mm) was simulated to mimic conventional transcranial Doppler imaging (Tsuchiya et al. 1991; Baumgartner et al. 1997; Lindsey et al. 2011; Lindsey and Smith 2013). The skull sample was scanned using microCT at a voxel size of 0.021 mm. Following the same procedure described above, the 2-D cross-section of the skull was used to simulate transcranial imaging at frequencies from 1.5–3 MHz. In this part, a 0.7-mm target with an acoustic impedance of 47.7 × 10^6 Rayl was simulated to form a strong reflecting target in the field of view (FOV). The 2-D grid spacing was reduced to 0.02 mm because of the decreased wavelength. The Courant–Friedrichs–Lewy number was set to 0.05.

All the *ex vivo* human skull samples used in this study were purchased from Skulls Unlimited International Inc. (Oklahoma City, OK, USA), a supplier of skulls for researchers; thus, no identifying information was collected and no institutional review board approval was required.

Experimental study

In the experimental study corresponding to the simulated imaging through the temporal bone, we

investigated the performance of transcranial ultrasound imaging through the *ex vivo* temporal bone sample at varying incidence angles. A linear array transducer (P4-1, ATL, Bothell, WA, USA) was used to image through the 3-mm-thick skull piece with transmit frequencies varying from 1.5−3 MHz. The images were acquired at incidence angles of 0˚, 15˚, 30˚ and 40˚. An air-filled polytetrafluoroethylene microtube (0.7-mm diameter) target was placed at a distance of 50 mm away from the transducer surface to produce a stable, strong reflection with a high SNR in the experimentally acquired images. The skull piece was placed 30 mm away from the transducer to allow enough space for varying the incidence angle while also preventing reverberation artifacts close to the skull and transducer from overlapping at the same depth as the target. To image through the skull sample at a location close to the same location as in the simulation study, a landmark on the bone surface (*i.e.,* bony ridge) identified in the CT image was identified in real-time ultrasound imaging by placing a metal wire maker in the location of this landmark. The wire was then removed before data acquisition. For each frequency and incidence angle, 100 frames of images were obtained for each of the two cases: with and without the target. Each image was obtained by using a single-plane-wave transmission without using multiple angle compounding. The final differential image (Fig. 3b) was obtained by calculating the difference between the in-phase and quadrature (IQ) data obtained with and without the target, then averaging across 100 frames to suppress the random noise. The combination of the strong reflecting target and the 100-frame averaging approach was designed to produce sufficient SNR to enable investigation of all phenomena of acoustic origin with minimal influence from the system noise. To measure the noise level of the differential imaging method and quantify the SNR, another set of differential images were obtained by calculating the difference between two sets of IQ data that were both acquired without deploying the hyperechoic target. This set of data is denoted as the noise image (Fig. 3c).

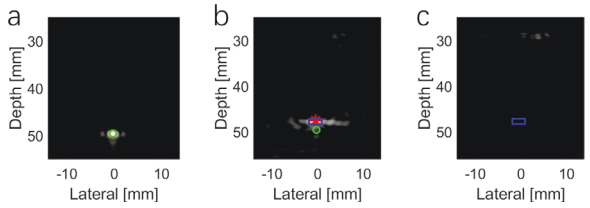

Fig. 3. Example of quantitative image analysis approach used in this work, shown without the skull. (a) B-Mode image of the single hyperechoic target without the skull. (b) The differential image of the target was obtained by calculating the difference between the two sets of in-phase and quadrature (IQ) data obtained with and without the target below the skull. (c) The noise image was obtained by calculating the difference between two sets of IQ data that are both acquired without the hyperechoic target. The *red star* indicates the location of the single target identified by finding the maximum pixel value. The *green circle* indicates the location of the ground truth location of the target identified in the image obtained without skull (a). The *blue rectangle* indicates the full width at half-maximum (FWHM) along the axial (*i.e.,* depth) and lateral directions measured in the differential image. Each image is normalized to the maximum pixel value and displayed in a dynamic range of 20 dB.

Quantitative image analysis

Imaging performance was evaluated for both aberration (*i.e.,* localization error) and spatial resolution. For determining localization errors, the location of the point target was identified by finding the pixel with the highest magnitude in the image (Fig. 3b) and comparing it with the image obtained without the skull (Fig. 3a) to calculate the shift error of the target. The shift errors along both the axial (*i.e.,* depth) and lateral directions were reported. The resolution was evaluated by calculating the full width at half maximum (FWHM, indicated by the blue rectangle in Fig. 3b) of the target in the image along both the axial and lateral directions. Comparisons of the absolute shift error along both the axial and lateral directions with the FWHM between different imaging angles and porosities were conducted using a one-way analysis of variance test. The difference between groups were considered significant when the p value was <0.05.

In the experimental study, the SNR values of images formed using the differential imaging strategy were quantified. In each image, the signal amplitude was the average signal amplitude in the −6-dB region in the differential image (Fig. 3b). The noise amplitude was measured as the average amplitude in the same region in the noise image (Fig. 3c).

RESULTS

Simulation of imaging through a bone plate phantom

As illustrated in all the images obtained at incidence angles of 0˚ and 15˚ (Fig. 4), the location of the point target shifted upward toward a shallower depth compared with the ground truth location of the target (*green circle*). As indicated by the quantitative results, the upward shift along the axial direction is between 2 and 4 mm at 0˚ and 15˚ across different porosities (Fig. 5a). When the incidence angle increased to 30˚, a shift was still seen across varying porosities, while the direction of the shift varied (Fig. 4g−i). At an incidence angle of 40˚ and porosities of 5.18% and 8.44%, the location of the target in the transcranial image shifted near the ground truth, indicating that the shift error decreased (Fig. 4j, 4k).

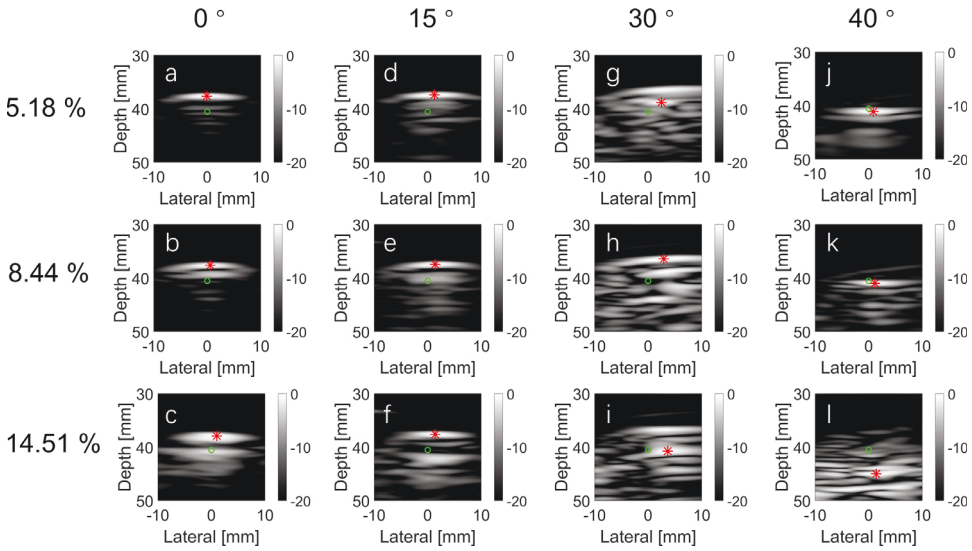

Fig. 4. Simulated transcranial images obtained using artificially generated skull plates. The *red star* indicates the location of the target, which was identified at the location of the peak pixel value in each image. The *green circle* indicates the ground truth location of the target identified in the image simulated without the skull. Each row was obtained at the same porosity level. Each column was obtained at the same incidence angle.

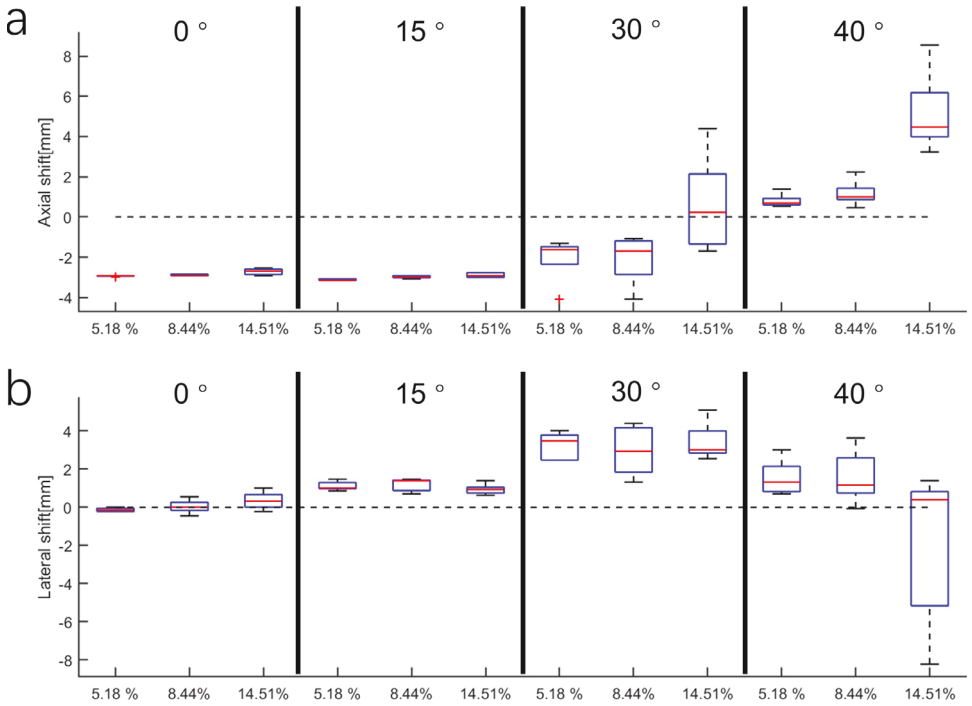

Fig. 5. (a) Axial and (b) lateral shift error quantified in the simulated transcranial images at three different levels of porosity (*i.e.,* 5.18%, 8.44%, 14.51%) and four different incidence angles (*i.e.,* 0˚, 15˚, 30˚, 40˚). The *black dashed line* indicates the 0-mm shift.

The size of the point target visualized in the image varied at different incidence angles and porosity levels (Fig. 4). The point target was visualized as a dense, high-contrast signal in the image at 0˚, especially at porosities of 5.18% and 8.44%. There were no significant differences in the axial and lateral extents between different porosities at 0˚ (Fig. 6). However, at both 15˚ and 30˚, the axial FWHM was significantly enlarged at a porosity of 14.51% ($p < 0.05$) compared with those of 5.18% and 8.44%. At 40˚, the point target was visualized in the image as different patterns of multiple points (rather than the single point target) at different

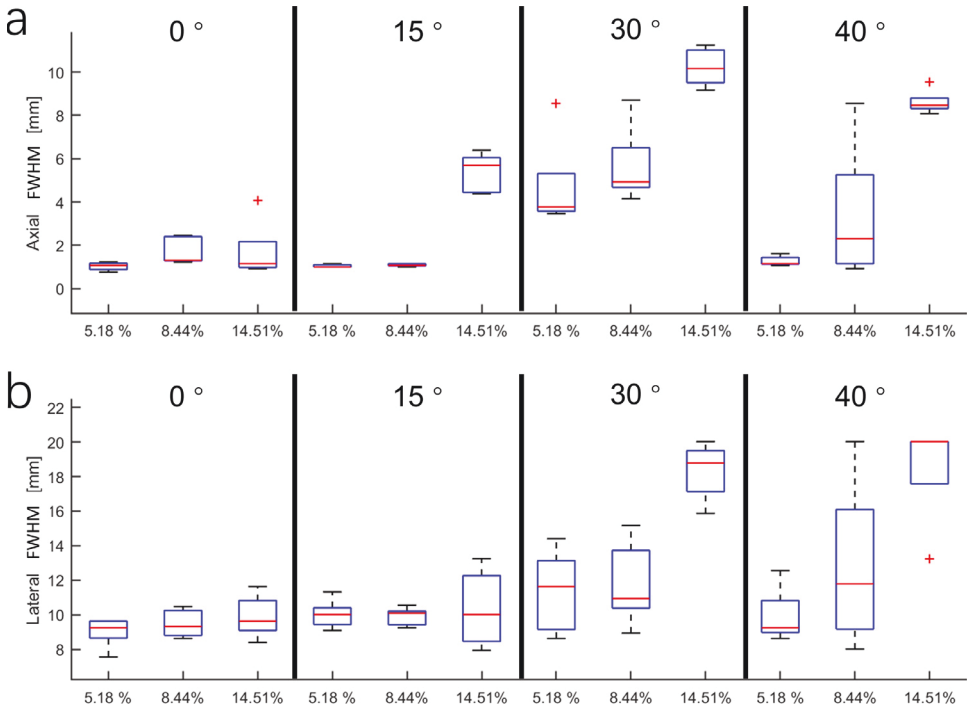

Fig. 6. (a) Axial and (b) lateral full width at half-maximum (FWHM) of the point target quantified in the simulated transcranial images at three different levels of porosity (*i.e.,* 5.18%, 8.44%, 14.51%) and four different incidence angles (*i.e.,* 0˚, 15˚, 30˚, 40˚).

porosities. At the lowest porosity level, imaging the point target through the skull resulted in a dense, coherent signal in the image (Fig. 4j), while at the highest porosity level, the point target resulted in a group of multiple points in the image (Fig. 4l). Quantitative results indicate that at 40˚, the axial size of the target at a porosity of 5.18% was <1.62 mm, which was significantly smaller than that (8.08−9.54 mm) at a porosity of 14.51% ($p < 0.05$). There was no significant difference in lateral FWHM between different incidence angles at porosities of 5.18% and 8.44%. At 40˚, the lateral FWHM was significantly enlarged at a porosity of 14.51% ($p < 0.05$), which was in accordance with the multiple target appearance seen in Figure 4l.

Simulated imaging through parietal bone

At 0˚, the point target shifted upward toward the transducer, as indicated by the *red star* (Fig. 7). When the incidence angle increased to 30˚ (*i.e.,* very close to the nominal critical angle of 30.8˚ when c_{skull} = 3000 m/s and c_{tissue} = 1540 m/s), it was not always feasible to detect the location of the point target within the simulated FOV at the highest level of porosity (26.9%) (Fig. 7i). When the incidence angle increased to 40˚ above the critical angle, the feasibility of identifying the point target location in the images differed across different levels of porosity. For both the full skull and the 13.45% porosity level, the identification of the point target was barely achievable as the peak intensity location shifted out of the FOV (Fig. 7m, 7n). Alternatively, the target was identified near the ground truth location of the target as indicated by the *red star* and *green circle* (ground truth) in Figure 7o and p at the lower levels of porosity (*i.e.,* 2.69% and 0%).

Similar to the results obtained in the artificially generated bone plate, the point target resulted in an image of a dense, hyperechoic target in the FOV at 0˚ with porosities of 0% and 2.69%. The axial FWHM of the target was <4.31 mm (Fig. 8a). When the large-incidence-angle (40˚) imaging method was used, the performance varied significantly across different porosities (Fig. 7m−p). At a porosity of 0% (*red dashed line*), the size of the axial FWHM was 1.15 mm (Fig. 8a), although the lateral spatial extent was 10.09 mm (Fig. 8b) at an incidence angle of 40˚. At a porosity of 2.69%, the axial spatial extent increased to 7.39 (varying from 4.46−10.08) mm. As the location of the peak intensity identified as the point target shifted out of the FOV because of the presence of the porous bone with porosities of 13.45% and 26.9%, quantification of the FWHM and the imaging resolution was not achievable in these cases.

Simulation and experimental studies of transcranial imaging through temporal bone window

In both the experimental and simulated images (Figs. 9 and 10), there was a shift of the target

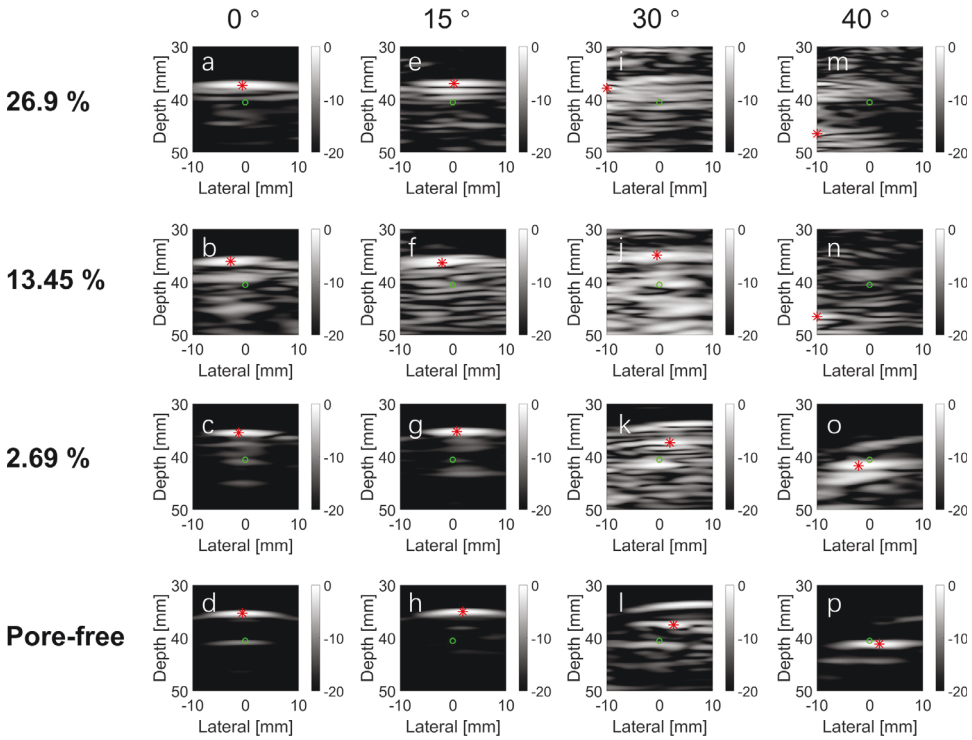

Fig. 7. Simulated transcranial images obtained using micro-computed tomography data of an *ex vivo* human skull. The *red star* indicates the location of the target, identified as the location of the peak pixel value in each image. The *green circle* indicates the ground truth location of the target identified in the image simulated without bone. Each row was obtained at the same porosity level. Each column was obtained at the same incidence angle.

identified in the images in the presence of the skull sample. When the images were obtained at 0° and 15°, the location of the target shifted upward toward the transducer (Fig. 9a–h). The axial shift induced by the skull ranged from −1.76 to −2.11 mm (Table 2). The target appeared as a dense, hyperechoic signal located at a depth between 45–50 mm. When the incidence angle increased to angles near or above the critical angle (*i.e.,* 30°, 40°), the microtubing target resulted in an image of a group of multiple targets located across a region from 45 to >50 mm deep. Localizing the target by finding the peak intensity location resulted in a significant lateral shift, as outlined in Table 2. In addition, the variation in transmit frequency within the range of 1.5–3 MHz did not have any significant impact on the imaging performance at large incidence angles.

In the simulated images obtained at 0° (Fig. 10), despite the reverberation below the hyperechoic target, the FWHMs of targets were ≤0.62 and ≤7.78 mm along axial and lateral directions, respectively. At 40°, the location of the target identified in the image shifted further away from the ground truth location. The FWHM increased to 4.54 mm axially and 13.86 mm laterally, which made localization of the target difficult.

DISCUSSION

Although there have been numerous studies of human skull properties for the purpose of aberration correction, there are only a limited number of reports of transcranial ultrasound propagation in which the role of the microstructure of the porous skull bone was investigated and none of them addresses imaging directly (Liu 2012; Pinton et al. 2012; Robertson et al. 2018; Webb 2018; Mazzotti et al. 2021b). To our knowledge, this is the first time that the effects of the microstructure of the human skull on transcranial ultrasound image quality have been studied.

An upward axial shift was seen in both simulation and experimental results when the image was obtained at an incidence angle of 0°. The shift error could be owing mainly to the aberration that occurred when a constant speed of sound was used to calculate the time delay for image reconstruction, while ultrasound traveled through the skull at a speed higher than the assumed speed of sound. The degree of axial shift was expected to be proportional to the mismatch between the average sound speed in the 6-mm-thick bone plate (Figs. 1, 4 and 5) and the assumed speed. However, there was no significant difference ($p > 0.05$) in axial shift error between all

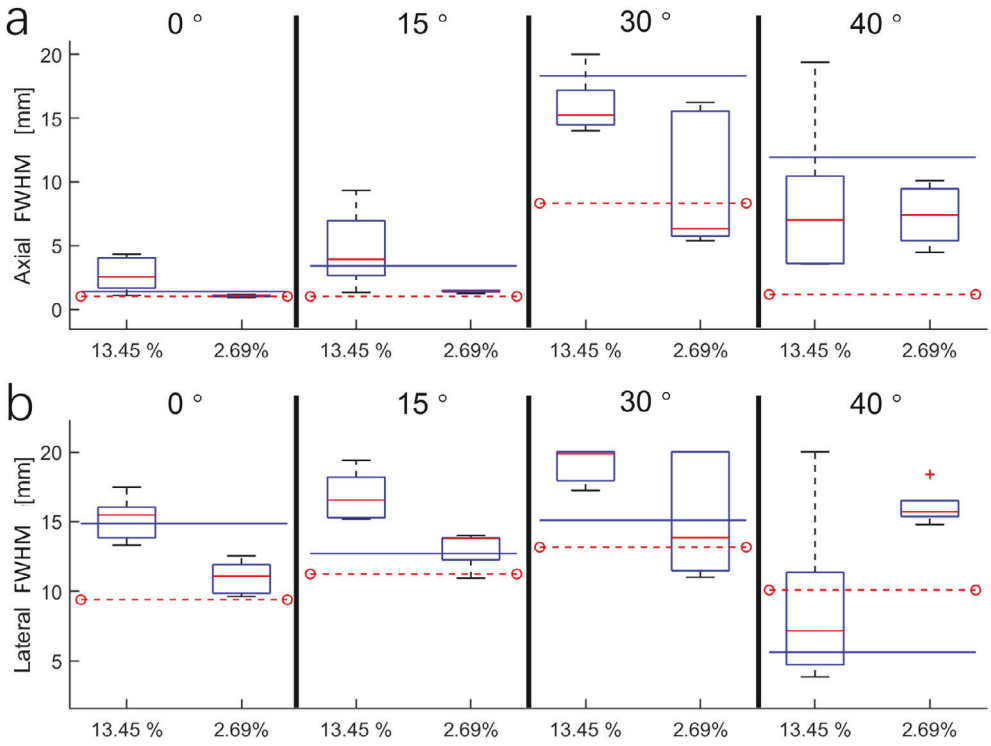

Fig. 8. (a) Axial and (b) lateral full width at half-maximum (FWHM) of the point target quantified in the simulated transcranial images using an *ex vivo* human skull at four different levels of porosity (*i.e.,* 26.9%, 13.45%, 2.69%, 0%) and four different incidence angles (*i.e.,* 0˚, 15˚, 30˚, 40˚). Because only one image was simulated for both the original skull with a porosity of 26.9% and the pore-free skull, the results are presented as a scalar number for each case. The *red dashed line* indicates the results obtained in the pore-free skull. The *blue line* indicates the results obtained in the original skull.

three levels of porosities (5.18 %, 8.44% and 14.51%) at 0˚ (Fig. 5a), indicating that the difference in the average speed of sound between different porosities was not significant. This implies that average sound speed depends on other factors more than porosity (Webb 2018), although porosity alone has been previously used to estimate the speed of sound for aberration correction in transcranial focused ultrasound (Clement and Hynynen 2002; Aubry et al. 2003).

In the simulation using the artificially generated bone plate, the axial shift at 40˚ (Fig. 4j) was significantly lower ($p < 0.05$) at a porosity of 5.18% than those of 0˚ and 15˚ images (Figs. 4a, 4d and 5a), which was consistent with the previous report that it is feasible to reduce the effects of aberration by increasing the incidence angle to large angles above the critical angle of longitudinal waves (30.8˚, calculated based on the longitudinal wave speed in water and bone) (Clement et al. 2004; Yousefi et al. 2009; Lucht et al. 2013). However, there was a significantly larger shift ($p < 0.05$) at a porosity level of 14.51% than at lower porosity levels (Fig. 5a, 40˚). For the skull samples with porosity levels of 5.18% and 8.44% imaged at 40˚, the lateral shift error was not significantly different from that at small angles (0˚ and 15˚), while for a porosity of 14.51%, there were cases with a lateral shift as large as 8.2 mm. Overall, the absolute error (calculated based on axial and lateral shifts) reached a minimum value of 0.93 mm at 40˚ for the bone with a porosity of 5.18%. The simulation of imaging through both the artificially generated bone plate (Fig. 5) and the parietal bone (Fig. 11) indicated that the feasibility of aberration reduction via increasing angle of incidence to introduce mode conversion depends on the microstructure (porosity) of the bone. Increasing the incidence angle did appear to reduce aberration effects at low porosity. However, at higher levels of porosity, increasing the angle of incidence resulted in large shift errors during point target localization. The results of the FWHM of the target (Fig. 6) also indicated that imaging resolution was highly dependent on the level of porosity, even when the influence of degradation of SNR was excluded in simulations. The feasibility of localizing even a strongly scattering point target through the skull in shear wave mode conversion imaging at large incidence angles depended heavily on the porosity of the skull.

In addition to the simulation study, the experimental results were obtained by imaging through a 3-mm

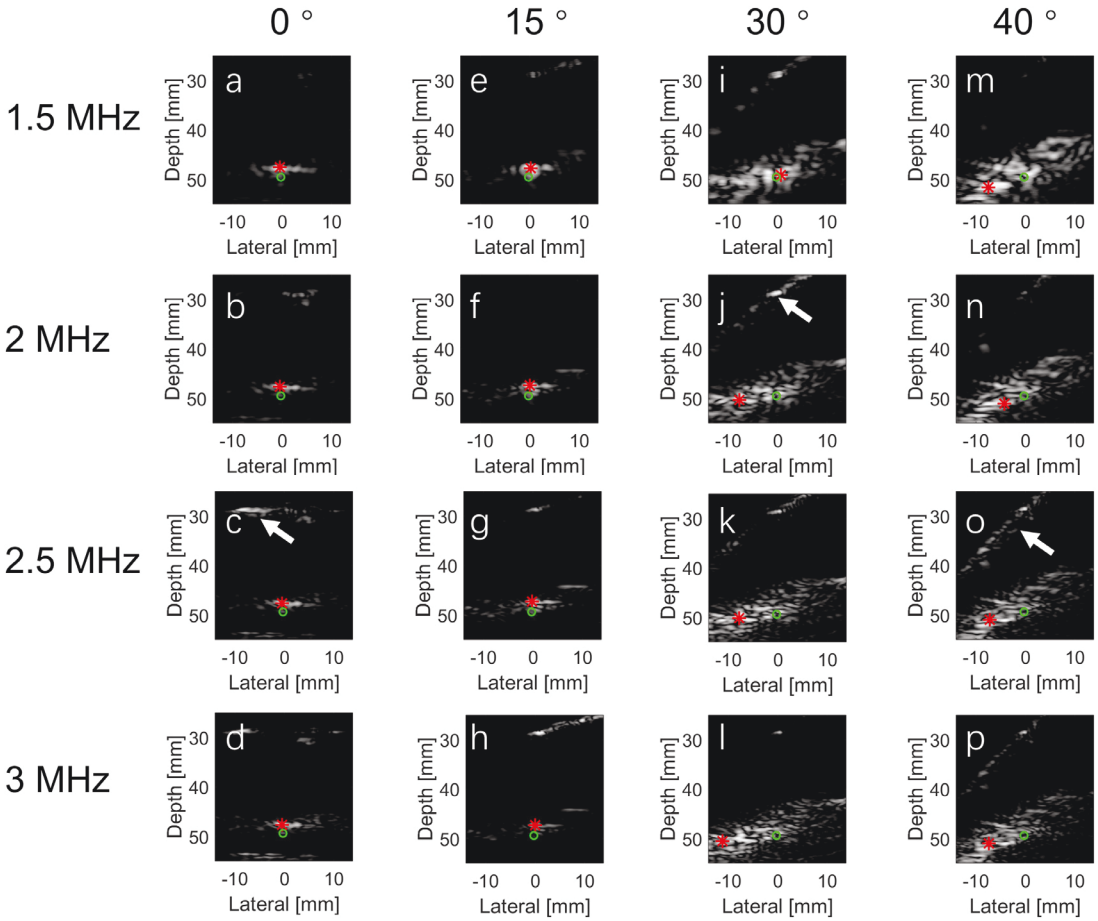

Fig. 9. Experimental transcranial images obtained using an *ex vivo* human skull piece at frequencies from 1.5 to 3 MHz and angles from 0° to 40°. The *red star* indicates the location of the target, which was identified as the location of the peak pixel value in each image. The *green circle* indicates the ground truth location of the target identified in the image acquired without the skull. Each row was obtained at the same frequency. Each column was obtained at the same incidence angle. The *white arrows* indicate the signal from the skull. Each image is normalized to the maximum pixel value and displayed in a dynamic range of 20 dB.

temporal bone. The multiple-target appearance in the transcranial ultrasound images in Figure 9i–p was similar to that in the images obtained in simulations when the porosity level increased (Figs. 4 and 7). It should be noted that these diffuse-appearing targets were not random noise and were visible only with the target, as the SNR measurement indicated that these diffuse-appearing targets were 37.51 to 42.40 dB above the noise level (Fig. 3c). Thus, the degradation of imaging SNR related to the acoustic attenuation can be ruled out as the cause of these incoherent diffusive-appearing objects in the images. While further study would be required to verify the cause definitively, the main cause of the loss of coherence could be multiple scattering at the interface between the bone and the pores.

Previous publications have reported that transcranial ultrasound imaging at large angles of incidence has successfully detected contrast agent-filled microtubing in 6 of 9 skulls at subharmonics (~375 kHz) and 1 of 9 at the fundamental frequency (750 Hz), while in the remaining skulls, the targets were not detectable in the images at large incidence angles (Lucht et al. 2013). The present study using simulations and a differential imaging strategy provides new insights into the efficiency of target detection and sources of image degradation at large angles of incidence. On the basis of this study, the inconsistency in target identification and localization across skulls could be owing to the incoherent scattering of the ultrasound wave in the presence of the porous structures inside the skull.

The current simulation was conducted in 2-D rather than 3-D space because of the enormous computational cost of the present acoustic simulation having high spatial and temporal resolution ($>10^6$ grid points, >20,000 time steps). In 3-D space, the porous network within the trabecular bone exhibits varying orientation and

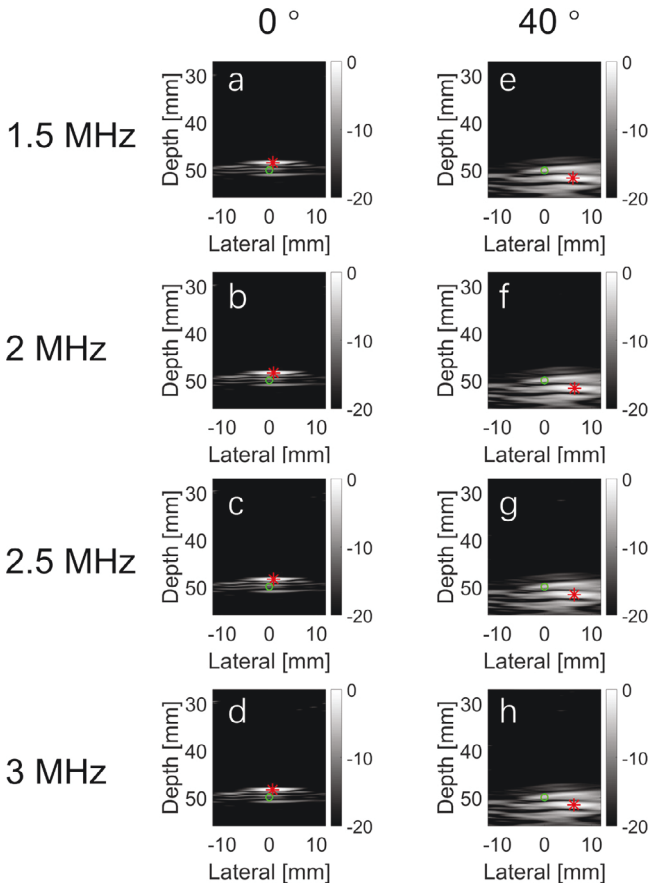

Fig. 10. Simulated transcranial images using the micro-computed tomography data of the skull sample in the experimental study. The *red star* indicates the location of the target, which was identified at the location of the peak pixel value in each image. The *green circle* indicates the ground truth location of the target identified in the image acquired without the skull. Each row was obtained at the same frequency. Each column was obtained at the same incidence angle.

Table 2. Quantitative measurements of the shift error and the FWHM of the target in the image

Frequency (MHz)	Angle			
	0°	15°	30°	40°
		Axial shift (mm)		
1.5	−1.99	−1.82	−0.41	2.05
2	−1.88	−2.11	0.82	1.58
2.5	−1.76	−2.05	0.76	1.64
3	−1.76	−2.11	1.11	1.64
		Lateral shift (mm)		
1.5	−0.23	0.46	0.87	−7.22
2	−0.17	0.29	−7.45	-3.95
2.5	−0.17	0.12	−7.56	−6.93
3	−0.17	0.23	−10.89	−7.1
		Axial FWHM (mm)		
1.5	1.17	1.93	8.8	13.14
2	0.82	1.35	8.57	6.86
2.5	0.82	1.23	10.97	7.62
3	0.82	1.17	10.97	7.45
		Lateral FWHM (mm)		
1.5	2.79	3.02	26.95	18.8
2	4.71	4.83	26.6	13.62
2.5	4.71	4.77	27.06	11.58
3	4.65	4.83	27.01	10.47

anisotropy (Chaffai et al. 2002), which was not simulated in the 2-D domain in this study. In addition, while a best attempt was made to spatially register transducer placement in ultrasound imaging with that in simulations based on microCT images, the registration between the 3-D microCT images and the 2-D ultrasound images is not perfect, which could be another source of differences between the images obtained in simulations and experiments (Fig. 9 vs. Fig. 10).

The acoustic properties, including sound speed and absorption, defined in this current simulation were in accordance with the previous report of the modeling of the absorption of longitudinal and shear waves in the skull (Pinton et al. 2012). Thanks to the high-resolution CT scan of the skull, the absorption term was modeled independently of the scattering-induced attenuation. However, as discussed in the previous report (Pinton et al. 2012), the absorption of the longitudinal and shear waves is not independently modeled. In the present study, the absorption was modeled using the classic Kelvin−Voigt model of viscoelasticity

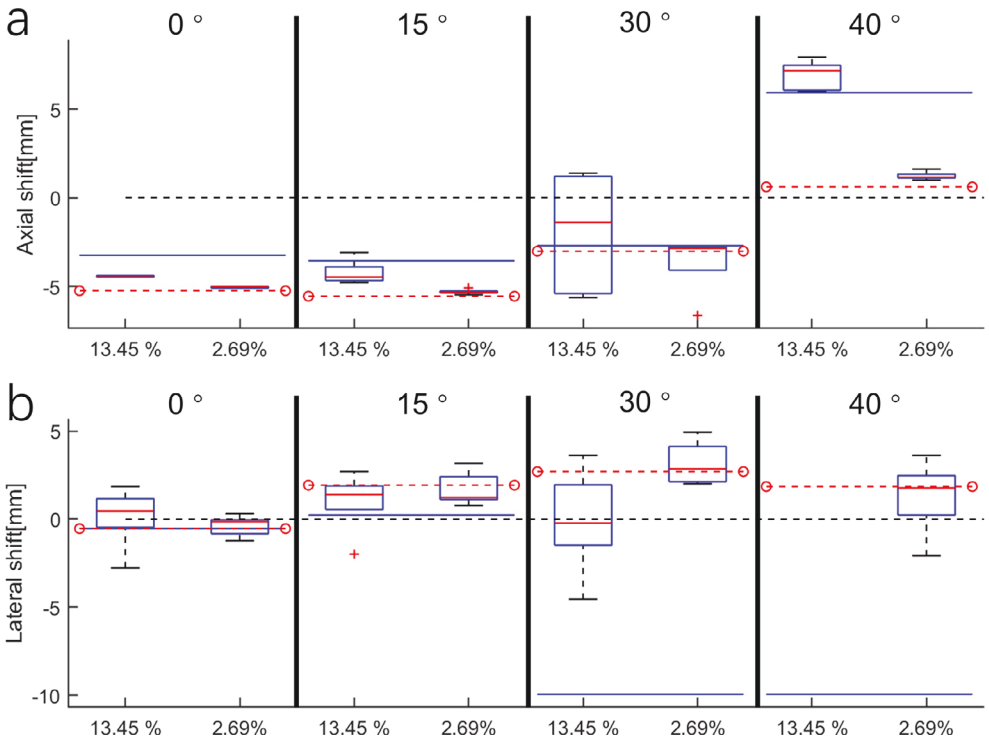

Fig. 11. (a) Axial and (b) lateral shift error quantified in the simulated transcranial images using an *ex vivo* human skull at four different levels of porosity (*i.e.,* 26.9%, 13.45%, 2.69%, 0%) and four different incidence angles (*i.e.,* 0˚, 15˚, 30˚, 40˚). Because only one image was simulated for both the original skull with a porosity of 26.9% and the pore-free skull, the results are presented as a scalar number for each case. *The red dashed line* indicates the results obtained in the pore-free skull. The *blue line* indicates the results obtained in the original skull. The *black dashed line* indicates the 0-mm shift.

(Treeby et al. 2014). The absorption coefficient was modeled to be proportional to frequency squared, which is different from the attenuation reported previously (White et al. 2006; Treeby and Cox 2014; Pichardo et al. 2017). However, it should be noted that measurements of the attenuation coefficient vary between different studies with different experimental setups. Unlike this study in which microCT was used to resolve the skull microstructure, in previous reports in which the attenuation coefficient was measured using models based on clinical CT data of the skull, these data represent the combination of absorption and other effects such as scattering and mode conversion at the trabecular porous structure (Aubry et al. 2003; Pichardo et al. 2011, 2017).

In this study, a limited number of skull samples were tested experimentally at transmit frequencies from 1.5−3 MHz. Testing at frequencies <1.5 MHz was not achievable because of the limited bandwidth of the commercially available array transducer. Further experimental studies are needed to validate the findings in the simulation at the low-frequency range (≤1 MHz), which may be of interest for several imaging applications and could be achieved by using customized, low-frequency transducer arrays (Lucht et al. 2013).

As described in the Results, there appear to be multiple reflections in these images, which could be owing to propagation of acoustic waves along different paths with varying velocities for different wave modes (*i.e.,* shear wave and longitudinal wave). In the present study, to determine the actual target among multiple target-like signals in the image, the peak was located, that is, the pixel with the highest magnitude. As the measurement of the localization error depends on the choice of target localization method, we also tested the method of computing the centroid instead of the peak to determine the target location to analyze the data in Figure 4. The localization error measurements did not significantly differ between these two methods of analysis, resulting in the same conclusion.

The simulation and experimental results reveal similar patterns in the variation of images of a single reflective target with increasing angle of incidence from normal to above the critical angle (Figs. 9 and 10). In the simulation study of the effect of porosity on imaging performance, the variation of localization shift error and resolution (FWHM) is smaller at 0˚ than that at 40˚ (Figs. 6−8), which indicates that the 0˚ (*i.e.,* longitudinal) imaging approach is less affected by the variation in the skull's microstructure than shear wave mode imaging at 40˚. The different

performance between small and large incidence angles may be attributed to the difference between the longitudinal and shear waves in interaction with the porous structure of the bone, which involves mode conversion and multiple scattering (Bossy et al. 2005; Wear 2020). It has been reported previously that improvement in imaging SNR could improve the detection rate of the shear wave mode converted transcranial imaging for some individual skulls (Yousefi et al. 2009; Lucht et al. 2013). Our study using both simulation and experimental approaches presents the first evidence that the detection and localization of the point target below the skull are highly dependent on the porosity of the skull even when the imaging SNR is sufficiently high, which might explain why improving imaging SNR alone is not enough to enable localization of the single hyperechoic target for some individual skulls.

It also should be noted that no post-processing methods were applied to realign the phase of the distorted wavefront (*i.e.,* aberration correction), as we are interested in examining the effect of varying incidence angle (*i.e.,* up to large angles to induce mode conversion) on the feasibility and accuracy of single-target localization. The improvement in image quality that could be achieved by realigning the phase of the received signal is unclear, however, based on both the simulation and experimental results, localization accuracy might be easy to improve in some skull specimens when the angle of incidence is 0° by compensating the upward shift error in beamforming. However, at non-normal angles of incidence, localizing the single target by realigning the wavefront in the presence of the multitarget artifact is likely unachievable, particularly in cases of larger angles of incidence, as illustrated in Figure 9i–p. At non-normal angles of incidence and as skull porosity increases, aberration correction becomes more challenging, requiring a time-reversal approach accounting for multiple scattering of the wavefront in the skull (Fink 1992).

The immediate indications of this present study include the following: (i) aberration reduction resulting from mode conversion depends on skull porosity, which must be accounted for in transcranial ultrasound imaging and transcranial focused ultrasound; (ii) skull microstructure needs to be accounted for when determining the transmitting angle of incidence and, therefore, the configuration of the transducer array position for imaging or therapeutic focusing on a specific brain region, for example, regions close to the skull. Although we only investigated the transcranial pulse-echo response to a single sub-wavelength hyperechoic target in this study, the findings regarding the dependence of imaging performance (*i.e.,* localization error, resolution) on skull porosity are also expected to remain valid in imaging diffuse or complex targets found in tissue such as brain vasculature (Tsuchiya et al. 1991; Lyden and Nelson 1997; Krejza et al. 1999; Lindsey and Smith 2013; Lindsey et al. 2011, 2013), microbubble contrast agents (Wiesmann et al. 2004; Bartels et al. 2005; Della Martina et al. 2005) and focused ultrasound-induced cavitation bubbles (Sukovich et al. 2020). This is also the first study to investigate the effects of skull microstructure on transcranial ultrasound imaging. Additionally, although this study is focused primarily on the effects of skull structure and incidence angle in two-way pulse-echo transmission, the observed effects on the porosity-dependent performance of mode-converted transcranial ultrasound imaging are also expected to apply to one-way transcranial focusing, that is, in transcranial ultrasound therapy and passive acoustic mapping. The variation of transcranial imaging performance across samples with the same porosity also indicates that a knowledge of skull micromorphology would be essential for techniques such as time-reversal transmit focusing (Fink 1992; Clement and Hynynen 2002; Aubry et al. 2003) in transcranial ultrasound therapy, especially when longitudinal-to-shear wave mode conversion is not negligible, which occurs at large incidence angles when focusing on targets near the skull.

CONCLUSIONS

Previous research has indicated the potential for reducing aberration in transcranial ultrasound focusing and imaging by intentionally increasing the incidence angle above the critical angle of the longitudinal wave. In this study, to better understand the fundamental mechanisms underlying the variation in imaging performance, the effect of the structure of the porous trabecular bone on transcranial imaging performance (*i.e.,* target localization errors and resolution) at varying incidence angles was investigated in elastic wave simulations and experiments. Simulation studies using high-resolution computed tomography indicated that the feasibility of aberration reduction via increasing angle of incidence to introduce mode conversion depends on the microstructure (porosity) of the bone. Increasing the incidence angle appeared to reduce aberration effects at low porosity. However, at higher levels of porosity, increasing the incidence angle resulted in large shift errors during point target localization and significant degradation of image resolution compared with imaging at normal incidence angle. Experimental investigation of varying angle of incidence also confirmed the findings of the simulation study.

CONFLICT OF INTEREST DISCLOSURE

The authors have no relevant conflicts of interest to disclose.

Acknowledgments—The authors thank Dr. Matteo Mazzotti for sharing the code to generate the skull plate phantom, Dr. Scott J. Schoen and Eetu A. Kohtanen for sharing the skull samples, Stephan Strassle Rojas for assisting in generation of the skull plate phantom and Dr.

Laxminarayanan Krishnan for his help with acquiring the microCT data of the skull sample. In addition, the authors thank Dr. Alper Erturk, Dr. Massimo Ruzzene and Dr. Costas Arvanitis for helpful discussions and suggestions in the course of these studies. This work was supported by National Science Foundation CMMI Award No. 1933158 on Coupling Skull−Brain Vibroacoustics and Ultrasound toward Enhanced Imaging, Diagnosis and Therapy. The content is solely the responsibility of the authors and does not necessarily represent the official views of the National Science Foundation.

REFERENCES

Antipova D, Eadie L, Makin S, Shannon H, Wilson P, Macaden A. The use of transcranial ultrasound and clinical assessment to diagnose ischaemic stroke due to large vessel occlusion in remote and rural areas. Plos One 2020;15 e0239653.

Arvanitis CD, McDannold N. Integrated ultrasound and magnetic resonance imaging for simultaneous temperature and cavitation monitoring during focused ultrasound therapies. Med Phys 2013;40 112901.

Aubry JF, Tanter M, Pernot M, Thomas JL, Fink M. Experimental demonstration of noninvasive transskull adaptive focusing based on prior computed tomography scans. J Acoust Soc Am 2003;113:84–93.

Bartels E, Henning S, Wellmer A, Giraldo-Velasquez M, Kermer P. Evaluation of cerebral perfusion deficit in stroke patients using new transcranial contrast imaging CPS technology—Preliminary results. Ultraschall Med 2005;26:478–486.

Baumgartner RW, Arnold M, Gonner F, Staikow I, Herrmann C, Rivoir A, Muri RM. Contrast-enhanced transcranial color-coded duplex sonography in ischemic cerebrovascular disease. Stroke 1997;28:2473–2478.

Bossy E, Padilla F, Peyrin F, Laugier P. Three-dimensional simulation of ultrasound propagation through trabecular bone structures measured by synchrotron microtomography. Phys Med Biol 2005;50:5545–5556.

Burgess MT, Apostolakis I, Konofagou EE. Power cavitation-guided blood-brain barrier opening with focused ultrasound and microbubbles. Phys Med Biol 2018;63 065009.

Chaffai S, Peyrin F, Nuzzo S, Porcher R, Berger G, Laugier P. Ultrasonic characterization of human cancellous bone using transmission and backscatter measurements: Relationships to density and microstructure. Bone 2002;30:229–237.

Chaplin V, Phipps MA, Caskey CF. A random phased-array for MR-guided transcranial ultrasound neuromodulation in non-human primates. Phys Med Biol 2018;63 105016.

Clement GT, Hynynen K. A non-invasive method for focusing ultrasound through the human skull. Phys Med Biol 2002;47:1219–1236.

Clement GT, White PJ, Hynynen K. Enhanced ultrasound transmission through the human skull using shear mode conversion. J Acoust Soc Am 2004;115:1356–1364.

Crake C, Brinker ST, Coviello CM, Livingstone MS, McDannold NJ. A dual-mode hemispherical sparse array for 3D passive acoustic mapping and skull localization within a clinical MRI guided focused ultrasound device. Phys Med Biol 2018;63 065008.

Della Martina A, Meyer-Wiethe K, Allemann E, Seidel G. Ultrasound contrast agents for brain perfusion imaging and ischemic stroke therapy. J Neuroimaging 2005;15:217–232.

Deng L, O'Reilly MA, Jones RM, An R, Hynynen K. A multi-frequency sparse hemispherical ultrasound phased array for microbubble-mediated transcranial therapy and simultaneous cavitation mapping. Phys Med Biol 2016;61:8476–8501.

Errico C, Osmanski BF, Pezet S, Couture O, Lenkei Z, Tanter M. Transcranial functional ultrasound imaging of the brain using microbubble-enhanced ultrasensitive Doppler. Neuroimage 2016;124:752–761.

Estrada H, Gottschalk S, Reiss M, Neuschmelting V, Goldbrunner R, Razansky D. Observation of guided acoustic waves in a human skull. Ultrasound Med Biol 2018;44:2388–2392.

Fink M. Time-reversal of ultrasonic fields: 1. Basic principles. IEEE Trans Ultrason Ferroelectr Freq Control 1992;39:555–566.

Firouzi K, Ghanouni P, Khuri-Yakub BT. 2017 Efficient transcranial ultrasound delivery via excitation of lamb waves: Concept and preliminary results. Proc IEEE Int Ultrason Symp 2017;1–4. doi: 10.1109/ULTSYM.2017.8092492.

Gahn G, Gerber J, Hallmeyer S, Hahn G, Ackerman RH, Reichmann H, von Kummer R. Contrast-enhanced transcranial color-coded duplexsonography in stroke patients with limited bone windows. Am J Neuroradiol 2000;21:509–514.

Herzberg M, Boy S, Holscher T, Ertl M, Zimmermann M, Ittner KP, Pemmerl J, Pels H, Bogdahn U, Schlachetzki F. Prehospital stroke diagnostics based on neurological examination and transcranial ultrasound. Crit Ultrasound J 2014;6:3.

Holscher T, Schlachetzki F, Zimmermann M, Jakob W, Ittner KP, Haslberger J, Bogdahn U, Boy S. Transcranial ultrasound from diagnosis to early stroke treatment: 1. Feasibility of prehospital cerebrovascular assessment. Cerebrovasc Dis 2008;26:659–663.

Imbault M, Chauvet D, Gennisson JL, Capelle L, Tanter M. Intraoperative functional ultrasound imaging of human brain activity. Sci Rep 2017;7:7304.

Ivancevich NM, Pinton GF, Nicoletto HA, Bennett E, Laskowitz DT, Smith SW. Real-time 3-D contrast-enhanced transcranial ultrasound and aberration correction. Ultrasound Med Biol 2008;34:1387–1395.

Jiang C, Li YQ, Li BY, Liu CC, Xu F, Xu KL, Ta DA. Ray theory-based transcranial phase correction for intracranial imaging: A phantom study. IEEE Access 2019;7:163013–163021.

Jing Y, Meral FC, Clement GT. Time-reversal transcranial ultrasound beam focusing using a *k*-space method. Phys Med Biol 2012;57:901–917.

Jing B, Arvanitis CD, Lindsey BD. Effect of incidence angle and wave mode conversion on transcranial ultrafast Doppler imaging. Proc IEEE Int Ultrason Symp (IUS) 2020;1–3. doi: 10.1109/IUS46767.2020.9251477.

Jones RM, O'Reilly MA, Hynynen K. Transcranial passive acoustic mapping with hemispherical sparse arrays using CT-based skull-specific aberration corrections: A simulation study. Phys Med Biol 2013;58:4981–5005.

Jones RM, Deng LL, Leung K, McMahon D, O'Reilly MA, Hynynen K. Three-dimensional transcranial microbubble imaging for guiding volumetric ultrasound-mediated blood−brain barrier opening. Theranostics 2018;8:2909–2926.

Jones RM, McMahon D, Hynynen K. Ultrafast three-dimensional microbubble imaging in vivo predicts tissue damage volume distributions during nonthermal brain ablation. Theranostics 2020;10:7211–7230.

Krejza J, Mariak Z, Walecki J, Szydlik P, Lewko J, Ustymowicz A. Transcranial color Doppler sonography of basal cerebral arteries in 182 healthy subjects: Age and sex variability and normal reference values for blood flow parameters. Am J Roentgenol 1999;172:213–218.

Kyriakou A, Neufeld E, Werner B, Szekely G, Kuster N. Full-wave acoustic and thermal modeling of transcranial ultrasound propagation and investigation of skull-induced aberration correction techniques: A feasibility study. J Ther Ultrasound 2015;3:11.

Lin HC, Fan CH, Ho YJ, Yeh CK. Dual-frequency chirp excitation for passive cavitation imaging in the brain. IEEE Trans Ultrason Ferroelectr Freq Control 2020;67:1127–1140.

Lindsey BD, Smith SW. Refraction correction in 3D transcranial ultrasound imaging. Ultrason Imaging 2014;36:35–54.

Lindsey BD, Light ED, Nicoletto HA, Bennett ER, Laskowitz DT, Smith SW. The ultrasound brain helmet: New transducers and volume registration for in vivo simultaneous multi-transducer 3-D transcranial imaging. IEEE Trans Ultrason Ferroelectr Freq Control 2011;58:1189–1202.

Lindsey BD, Smith SW. Pitch-Catch Phase Aberration Correction of Multiple Isoplanatic Patches for 3-D Transcranial Ultrasound Imaging. IEEE Trans Ultrason Ferroelectr Freq Control 2013;60:463–480.

Lindsey BD, Nicoletto HA, Bennett ER, Laskowitz DT, Smith SW. Simultaneous bilateral real-time 3-D transcranial ultrasound imaging at 1 MHz through poor acoustic windows. Ultrasound Med Biol 2013;39:721–734.

Liu J. Interaction of transcranial ultrasound with skull bones and microbubbles for treatment of ischemic stroke. University of Nebraska—Lincoln; 2012.

Liu HL, Tsai CH, Jan CK, Chang HY, Huang SM, Li ML, Qiu WB, Zheng HR. Design and implementation of a transmit/receive ultrasound phased array for brain applications. IEEE Trans Ultrason Ferroelectr Freq Control 2018;65:1756–1767.

Lucht B, Hubbell A, Hynynen K. Contrast-enhanced transcranial two-dimensional ultrasound imaging using shear-mode conversion at low frequency. Ultrasound Med Biol 2013;39:332–344.

Lyden PD, Nelson TR. Visualization of the cerebral circulation using three−dimensional transcranial power doppler ultrasound imaging. J Neuroimaging 1997;7:35–39.

Marinoni M, Ginanneschi A, Forleo P, Amaducci L. Technical limits in transcranial Doppler recording: Inadequate acoustic windows. Ultrasound Med Biol 1997;23:1275–1277.

Mazzotti M, Sugino C, Kohtanen E, Erturk A, Ruzzene M. Experimental identification of high order lamb waves and estimation of the mechanical properties of a dry human skull. Ultrasonics 2021a;113 106343.

Mazzotti M, Kohtanen E, Erturk A, Ruzzene M. Radiation characteristics of cranial leaky Lamb waves. IEEE Trans Ultrason Ferroelectr Freq Control 2021b;68:2129–2140.

O'Reilly MA, Hynynen K. A super-resolution ultrasound method for brain vascular mapping. Med Phys 2013;40 110701.

O'Reilly MA, Jones RM, Hynynen K. Three-dimensional transcranial ultrasound imaging of microbubble clouds using a sparse hemispherical array. IEEE Trans Biomed Eng 2014;61:1285–1294.

Pichardo S, Hynynen K. Treatment of near-skull brain tissue with a focused device using shear-mode conversion: A numerical study. Phys Med Biol 2007;52:7313–7332.

Pichardo S, Sin VW, Hynynen K. Multi-frequency characterization of the speed of sound and attenuation coefficient for longitudinal transmission of freshly excised human skulls. Phys Med Biol 2011;56:219–250.

Pichardo S, Moreno-Hernandez C, Drainville RA, Sin V, Curiel L, Hynynen K. A viscoelastic model for the prediction of transcranial ultrasound propagation: Application for the estimation of shear acoustic properties in the human skull. Phys Med Biol 2017;62:6938–6962.

Pinton G, Aubry JF, Bossy E, Muller M, Pernot M, Tanter M. Attenuation, scattering, and absorption of ultrasound in the skull bone. Med Phys 2012;39:299–307.

Preston C, Alvarez AM, Barragan A, Becker J, Kasoff WS, Witte RS. High resolution transcranial acoustoelectric imaging of current densities from a directional deep brain stimulator. J Neural Eng 2020;17 016074.

Qiu W, Bouakaz A, Konofagou EE, Zheng H. Ultrasound for the brain: A review of physical and engineering principles, and clinical applications. IEEE Trans Ultrason Ferroelectr Freq Control 2021;68:6–20.

Robertson J, Martin E, Cox B, Treeby BE. Sensitivity of simulated transcranial ultrasound fields to acoustic medium property maps. Phys Med Biol 2017a;62:2559–2580.

Robertson JLB, Cox BT, Jaros J, Treeby BE. Accurate simulation of transcranial ultrasound propagation for ultrasonic neuromodulation and stimulation. J Acoust Soc Am 2017b;141:1726–1738.

Robertson J, Urban J, Stitzel J, Treeby BE. The effects of image homogenisation on simulated transcranial ultrasound propagation. Phys Med Biol 2018;63 145014.

Schlachetzki F, Herzberg M, Holscher T, Ertl M, Zimmermann M, Ittner KP, Pels H, Bogdahn U, Boy S. Transcranial ultrasound from diagnosis to early stroke treatment: Part 2. Prehospital neurosonography in patients with acute stroke—The Regensburg Stroke Mobile Project. Cerebrovasc Dis 2012;33:262–271.

Schoen S, Arvanitis CD. Heterogeneous angular spectrum method for trans-skull imaging and focusing. IEEE Trans Med Imaging 2020;39:1605–1614.

Soulioti DE, Espindola D, Dayton PA, Pinton GF. Super-resolution imaging through the human skull. IEEE Trans Ultrason Ferroelectr Freq Control 2020;67:25–36.

Sukovich JR, Macoskey JJ, Lundt JE, Gerhardson TI, Hall TL, Xu Z. Real-time transcranial histotripsy treatment localization and mapping using acoustic cavitation emission feedback. IEEE Trans Ultrason Ferroelectr Freq Control 2020;67:1178–1191.

Sun T, Zhang YZ, Power C, Alexander PM, Sutton JT, Aryal M, Vykhodtseva N, Miller EL, McDannold NJ. Closed-loop control of targeted ultrasound drug delivery across the blood−brain/tumor barriers in a rat glioma model. Proc Natl Acad Sci USA 2017;114:E10281–E10290.

Treeby BE, Cox BT. Modeling power law absorption and dispersion in viscoelastic solids using a split-field and the fractional Laplacian. J Acoust Soc Am 2014;136:1499–1510.

Treeby BE, Jaros J, Rohrbac D, Cox BT. Modelling elastic wave propagation using the *k*-wave MATLAB Toolbox. Proc IEEE Int Ultrason Symp (IUS) 2014;146–149.

Tsuchiya T, Yasaka M, Yamaguchi T, Kimura K, Omae T. Imaging of the basal cerebral-arteries and measurement of blood velocity in adults by using transcranial real-time color Flow Doppler sonography. Am J Neuroradiol 1991;12:497–502.

Vignon F, Shi WT, Yin XT, Hoelscher T, Powers JE. The stripe artifact in transcranial ultrasound imaging. J Ultras Med 2010;29:1779–1786.

Wear KA. Mechanisms of interaction of ultrasound with cancellous bone: A review. IEEE Trans Ultrason Ferroelectr Freq Control 2020;67:454–482.

Webb TD. Predicting the transmission of ultrasound through the skull: Estimation of the acoustic properties of bone using computed tomography and magnetic resonance imaging. Dissertation. Stanford University; 2018.

White PJ, Clement GT, Hynynen K. Longitudinal and shear mode ultrasound propagation in human skull bone. Ultrasound Med Biol 2006;32:1085–1096.

Wiesmann M, Meyer K, Albers T, Seidel G. Parametric perfusion imaging with contrast-enhanced ultrasound in acute ischemic stroke. Stroke 2004;35:508–513.

Wu SY, Aurup C, Sanchez CS, Grondin J, Zheng WL, Kamimura H, Ferrera VP, Konofagou EE. Efficient blood−brain barrier opening in primates with neuronavigation-guided ultrasound and real-time acoustic mapping. Sci Rep 2018;8:7978.

Wu N, Shen G, Qu X, Wu H, Qiao S, Wang E, Chen Y, Wang H. Design of a versatile angle-rotatable skull-shaped conformal transcranial focused ultrasound transducer for noninvasive brain therapy. IEEE Trans Ultrason Ferroelectr Freq Control 2021;68:116–126.

Xu SS, Ye DZ, Wan L, Shentu YJ, Yue YM, Wan MX, Chen H. Correlation between brain tissue damage and inertial cavitation dose quantified using passive cavitation imaging. Ultrasound Med Biol 2019;45:2758–2766.

Yang YH, Zhang XH, Ye DZ, Laforest R, Williamson J, Liu YJ, Chen H. Cavitation dose painting for focused ultrasound-induced blood-brain barrier disruption. Sci Rep 2019;9:2840.

Yousefi A, Goertz DE, Hynynen K. Transcranial shear-mode ultrasound: Assessment of imaging performance and excitation techniques. IEEE Trans Med Imaging 2009;28:763–774.